

# Application of 2D acoustic frequency-domain full-waveform inversion to OBC wide-aperture data from the Valhall field

V. Prioux<sup>1</sup>, R. Brossier<sup>2</sup>, J.H. Kommedal<sup>3</sup>, O.I. Barkved<sup>3</sup>, S. Operto<sup>1</sup> and J. Virieux<sup>2</sup>

<sup>1</sup>Géoazur - CNRS - Univ Nice Sophia-Antipolis, <sup>2</sup>LGIT - Univ Joseph Fourier, <sup>3</sup>BP Norway

## SUMMARY

We present an application of 2D acoustic frequency-domain Full Waveform Inversion (FWI) to the hydrophone component of 4-C ocean bottom cable (OBC) data recorded from the Valhall field in North sea. The starting model for FWI was built by reflection traveltome tomography (RTT). Although this starting model leads to flat common-image gathers (CIGs), it does not allow us to match first-arrival traveltimes of diving waves from above the gas layers. This mismatch between vertical and horizontal velocities is likely the footprint of anisotropy. We updated the RTT model by first-arrival traveltome tomography (FATT) to build a new starting model for FWI. The velocities above the gas layers of the updated model are significantly higher than velocities from in-well seismic (VSP) data. FWI models were computed from the two starting models just mentioned. More stable results were obtained with the starting model updated by FATT. The resulting FWI model shows a reasonable agreement with a former model developed by 3D FWI. A reasonable match of both short-aperture and wide-aperture components of the data was obtained by isotropic FWI. This might indicate that layer-induced anisotropy was created by FWI in the gas layers to balance the increase of the shallow velocities created by the inversion of the wide-aperture data components.

## INTRODUCTION

Frequency-domain full-waveform inversion (FWI) is an efficient multiscale data-fitting approach for velocity model building from wide-aperture/ wide-azimuth acquisition geometries (Pratt and Worthington, 1990). In this study, we present an application of 2D frequency-domain acoustic FWI to a 2D dataset recorded by an ocean bottom cable (OBC) survey from the Valhall field (Kommedal et al., 2004)(Figure 1). Application of 3D acoustic frequency-domain FWI to the OBC data set was already presented by Sirgue et al. (2009, 2010) who built a high-resolution velocity model from low frequencies (3.5 - 7 Hz). The starting model for FWI was built by reflection traveltome tomography. The FWI velocity model clearly shows a series of channel complexes at 150-m depth and the low-velocity gas cloud above the reservoir level. Improved migrated images of the reservoir level and of the overburden were computed from the FWI velocity model. Although our study is limited to the 2D approximation, we want to assess in more details the sensitivity of the FWI to the starting model and assess to which extent acoustic FWI allows us to match wide-aperture data from the OBC survey in the isotropic approximation. We use seismic modeling, CIG analysis and comparison between VSP and FWI logs to assess the FWI models and the footprint of either intrinsic or layer-induced anisotropy in the imaging.

## METHOD

In this study, FWI is performed in the frequency domain following an efficient multiscale approach (Pratt and Worthington, 1990): only few increasing frequencies are successively inverted to inject progressively higher wavenumbers in the subsurface model. We use the  $L_1$  norm as the minimization functional in the data space. The  $L_1$  norm, that has been shown to be less sensitive to noise in the framework of efficient frequency-domain FWI (Brossier et al., 2009a), is defined by

$$\mathcal{G}_{L_1}^{(k)} = \sum_{i=1,N} |s_{d_i} \Delta d_i|, \quad (1)$$

where  $|x| = (xx^*)^{1/2}$ ,  $N$  is the number of elements in the misfit vector for one source and one frequency, and  $s_{d_i}$  control the respective weight of each element of the misfit vector. The gradient of the misfit function is given by

$$\mathcal{G}_{L_1}^{(k)} = \mathcal{R} \left\{ \mathbf{J}^t \mathbf{S}_d^t \mathbf{r} \right\} \quad \text{with } r_i = \frac{\Delta d_i^*}{|\Delta d_i|} \quad \text{for } 1 \leq i \leq N, \quad (2)$$

where we assume that  $|\Delta d_i| > 0$ , considering the machine precision used. The optimization relies on the L-BFGS algorithm (Nocedal, 1980) preconditioned by the diagonal terms of the Hessian. Seismic modeling is performed with a discontinuous Galerkin method on unstructured triangular mesh which allows for accurate positioning of sources and receivers and accurate parameterization of bathymetry (Brossier et al., 2009b).

## FWI PREPROCESSING AND EXPERIMENTAL SETUP

The dataset recorded by the cable 21 that we considered, consists of 320 shots recorded by 220 4-C components (Figure 1). We use only the hydrophone for acoustic FWI (Figure 2). Acoustic FWI was applied to the hydrophone component of elastic data computed in the synthetic elastic Valhall model and successfully imaged the  $V_P$  model (Brossier et al., 2009b). In virtue of the source-receiver reciprocity, the data are sorted by receiver gathers for FWI. The FWI preprocessing consists of spectral deconvolution, Butterworth filtering, 3D-to-2D correction and FK filtering of converted PS waves. Four frequencies (4, 5, 6 and 7 Hz) were successively inverted. The inverted data are tapered by a decreasing exponential function given by  $e^{-(t-t_0)/\tau}$  to limit the amount of late-arriving phases involved in the inversion. Here,  $t_0$  denotes the first-arrival time and we use  $\tau = 1$  s. Only the P-wave velocity is involved during the inversion and the density is updated once the first iteration using a Gardner law. A source wavelet per receiver gather is estimated during FWI from the data using a (linear) L2 estimation following Pratt (1999). The starting velocity model for FWI was built by reflection traveltome tomography

(RTT) (Figure 3a) (referred to as the RTT model in the following). Seismograms computed in the RTT model show significant mismatch with the first arrivals of the recorded data (Figure 4a). This mismatch prompts us to update the RTT model by FATT (referred to as FATT model in the following) (Figure 3b). Match of the first-arrival traveltimes leads to higher velocities in the first 1500 meters of the model (Figure 5). Seismograms computed in the FATT model show a good match of the observed first-arrival traveltimes (Figure 4b). However, the kinematic of the reflections from the deep part of the model was indeed affected by the update of the shallow velocities.

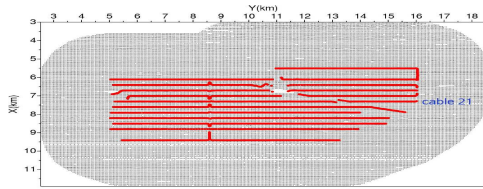


Figure 1: Layout of the Valhall zone (from Sirgue et al., 2009, 2010).

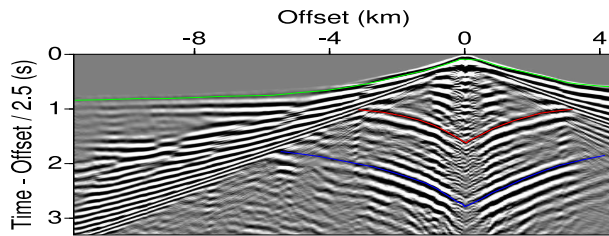


Figure 2: Example of recorded receiver gather. The green curve corresponds to manually-picked first-arrival traveltimes associated with diving waves from above the gas layers. The red and blue curves are inferred from rough picking of reflected waves from the top and the bottom of the gas layers. Seismograms are plotted with a reduction velocity of 2.5 km/s.

## FWI RESULTS

We apply acoustic frequency-domain FWI using the RTT and the FATT models as starting velocity models. The final FWI models derived from the RTT and FATT models (referred to as the RTT-FWI model and the FATT-FWI model, respectively) are shown in Figures 6(a-b). A sharp reflector at 0.4-km depth and some layering in the gas layers are imaged in the final FWI models. Some shallow artifacts near the ends of the ocean bottom cable result from the incomplete receiver coverage near the end of the profile.

Velocities above the gas layers from the RTT-FWI model show a good agreement with that of the well log but sharp layering with lower velocities than expected was created in the gas (Figure 5b). In contrast the FATT-FWI model shows higher velocities above the gas but a good agreement with well velocities is shown in the gas layers (Figure 5a). To appraise the relevance of the final FWI velocity models, we first compute source wavelets associated with each receiver gather in

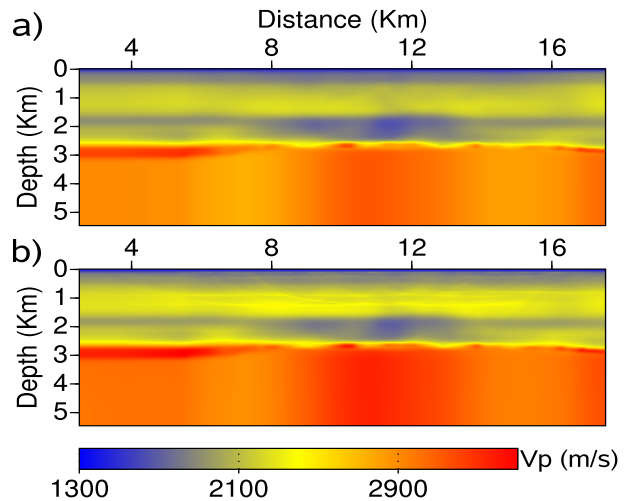


Figure 3: (a) RTT velocity model. (b) FATT velocity model. The low velocity zone between 1.7 and 2.5 km depth corresponds to the gas area above the reservoir level.

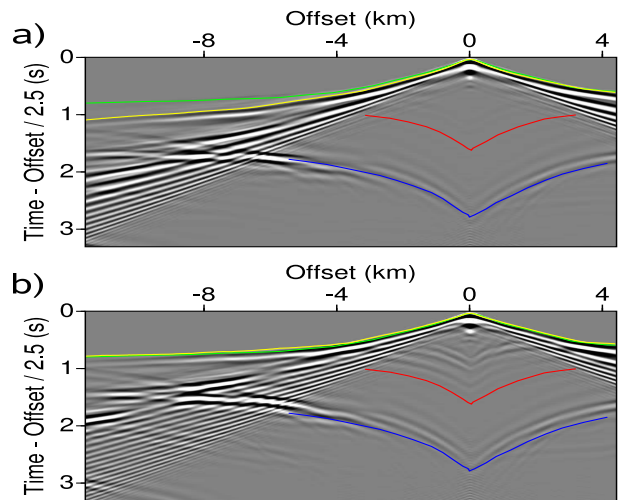


Figure 4: (a) Receiver gather computed in the RTT model. The yellow and the green curves represent the first arrivals computed in the RTT model and the first arrivals manually picked on the data, respectively. Note the mismatch between the two curves. (b) Receiver gather computed in the FATT model.

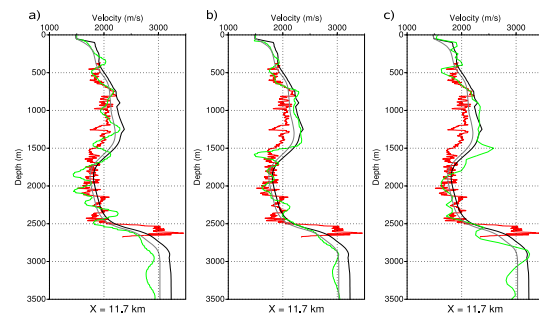


Figure 5: Velocity logs from the FATT model (gray), from the RTT model (black), and from the well (red). Logs from the FWI models are shown in green. (a) FATT-FWI model, (b) RTT-FWI model, (c) 3D model from Sirgue et al. (2009).

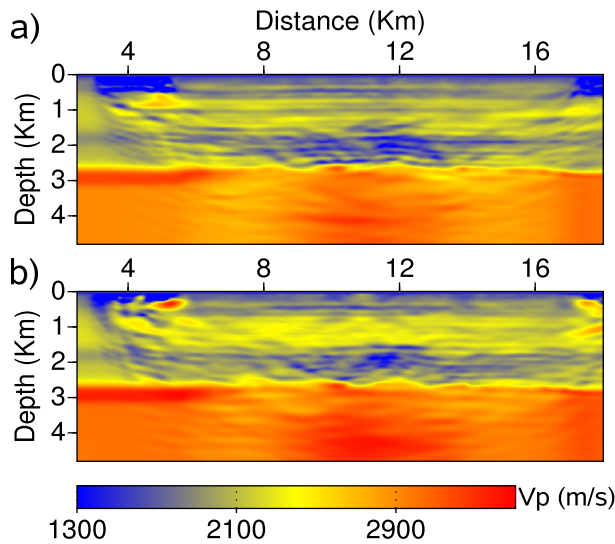


Figure 6: Final FWI models using as starting model (a) the RTT model and (b) the FATT model.

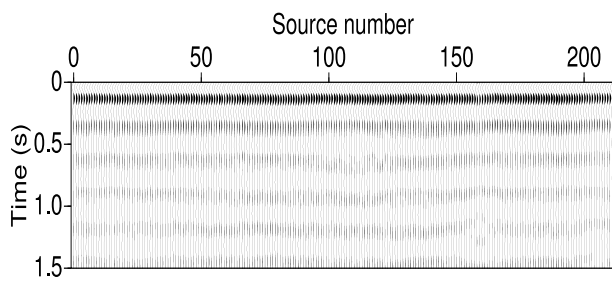


Figure 7: Source wavelet estimated for each receiver gather from the FATT-FWI velocity model.

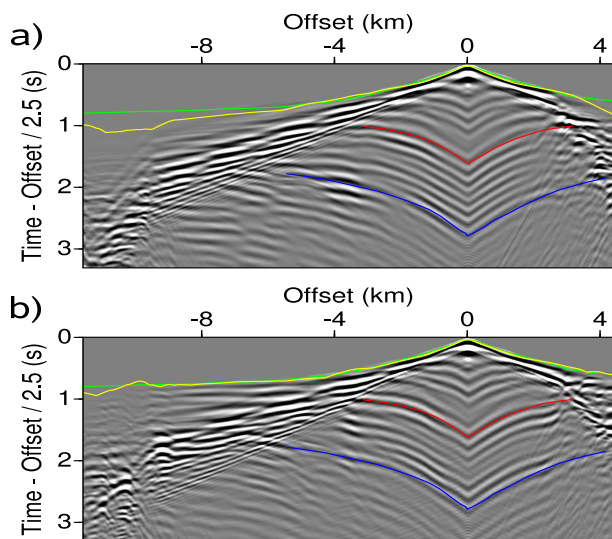


Figure 8: Receiver gathers computed in (a) the RTT-FWI and (b) the FATT-FWI models.

the time domain by solving a linear inverse problem at each frequency (Pratt (1999), his equation 17). The functional of the linear inverse problem is given by  $\mathcal{C} = \|\mathbf{d}_{obs} - \mathbf{sg}\|_{L_1/L_2}$ , where  $g$  denotes Green function and  $s$  is the complex-valued source term at one frequency. The source wavelet was estimated within the 4-20 Hz frequency bandwidth. Source wavelets are estimated with the  $L_1$  norm using a Very Fast Simulating Annealing algorithm (Sen and Stoffa, 1995) and with the  $L_2$  norm. Both functionals give similar source wavelets. The source wavelets estimated for each receiver gather have a similar waveform and amplitude (Figure 7) which provides a first argument in favor of the relevance of the FWI model. The source wavelets shown in Figure 7 were used to compute time-domain seismograms in the FWI models. Synthetic receiver gathers computed in the RTT- and FATT-FWI models are shown in Figure 8, and can be compared with the recorded receiver gather shown in Figure 2. The modeled seismograms are significantly affected at long offsets by the shallow artifacts shown in Figure 6. Direct comparisons between recorded and modeled seismograms show that the RTT-FWI model allows us to match the deep reflected wavefield, unlike the first arrivals which show significant mismatch (Figure 9a)). In contrast, the FATT-FWI model provides a reasonable match of both the reflected and refracted wavefields (Figure 9b).

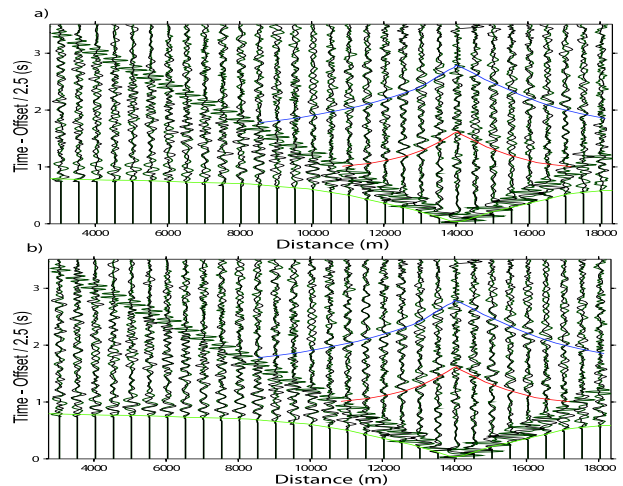


Figure 9: Direct comparison between the recorded data (in green) and modeled data (in black) computed in the FWI models. (a) FWI-RTT model. (b) FWI-FATT model. An automatic gain control was applied to the amplitudes. The time scale is plotted with a reduction velocity of 2.5 km/s

To further assess the relevance of the FWI models, we computed ray+Born depth migrated images and common image gathers (CIGs) for the RTT and FATT models as well as for the corresponding FWI models. Most of the CIGs in the RTT model are flat (Figure 10), and FWI does not allow us to improve these CIGs (Figure 11). The CIGs computed in the FATT model are degraded compared to that inferred from the RTT model (Figure 12). However, the CIGs inferred from the FATT model were significantly improved after FWI (Figure 13) although they remain less accurate than that inferred from the RTT model.

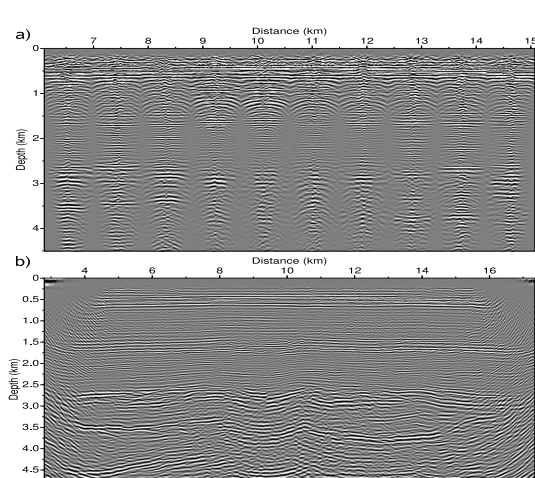


Figure 10: RTT model. (a) CIGs with a range of angles between  $-60^\circ$  to  $60^\circ$ , and whose position is given by the horizontal axis. (b) migrated image.

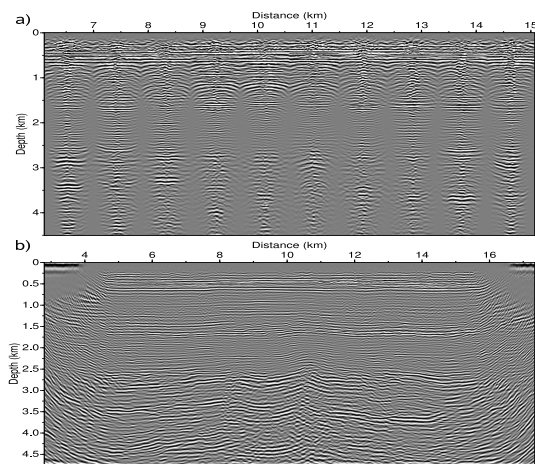


Figure 11: Same as Fig. 10 for the RTT-FWI model.

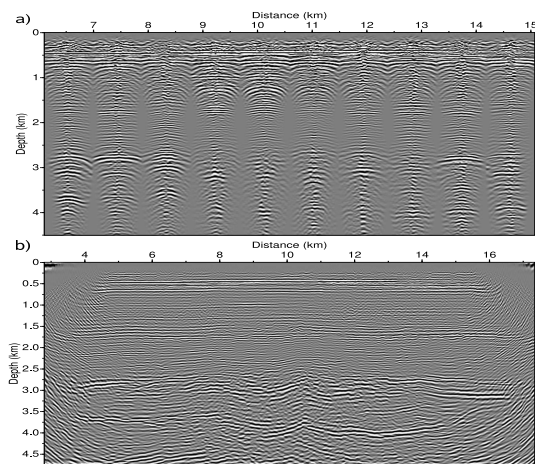


Figure 12: Same as Fig. 10 for the FATT model.

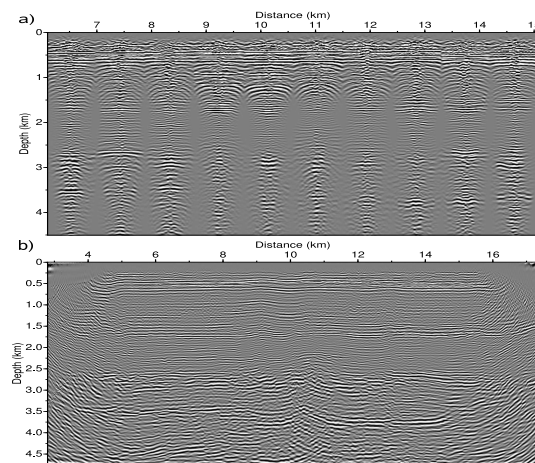


Figure 13: Same as Fig. 10 for FATT-FWI model.

## DISCUSSION AND CONCLUSION

Seismic modeling showed that the RTT velocity model does not allow for the match of the first arrivals of the Valhall data, although the RTT velocities show a good agreement with in-well (vertical) velocities (Figures 4a and 5). Higher velocities, introduced by FATT and FWI above the gas layers to match early-arriving waves, probably highlights the footprint of the anisotropy in the first 1.5 km of the medium. Match of the reflections from the top and bottom of the gas layers achieved by the FATT-FWI model was slightly degraded compared to that achieved with the RTT-FWI model but remains acceptable. This might suggest that FWI introduces fine-scale layering in the gas layers to generate layer-induced anisotropy (Pratt et al., 2001) that balances the increase of velocities introduced in the shallow part. Comparison between velocity profiles extracted from our FWI models and from the 3D acoustic (isotropic) FWI model of Sirgue et al. (2009, 2010) is shown in Figure 5. The FWI model of Sirgue et al. (2009, 2010) was inferred from the RTT model as starting model. The FWI model of Sirgue et al. (2009, 2010) also led to higher velocities in the shallow part compared to well-log velocities to match the first arrivals, that is consistent with our FATT-FWI model. To further verify the footprint of intrinsic and layer-induced anisotropy in FWI proposed in this study, application of 3D anisotropic FWI should be applied to the Valhall data set.

## ACKNOWLEDGMENTS

This study has been funded by the SEISCOPE consortium (<http://seiscope.oca.eu>), sponsored by BP, CGG-VERITAS, EXXON-MOBIL, SHELL and TOTAL. Access to the high-performance computing facilities of MESOCENTRE SIGAMM (OCA) and IDRIS (CNRS) computer centers provided the required computer resources. We would like to thank U. Albertin (BP), L. Sirgue (BP, now at Total) and R. E. Plessix (Shell) for fruitful comments and discussions. We thank BP Norge AS, Hess Norge, Total E and P Norge AS, and A/S Norske Shell for providing the Valhall data set.

## EDITED REFERENCES

Note: This reference list is a copy-edited version of the reference list submitted by the author. Reference lists for the 2010 SEG Technical Program Expanded Abstracts have been copy edited so that references provided with the online metadata for each paper will achieve a high degree of linking to cited sources that appear on the Web.

## REFERENCES

- Brossier, R., S. Operto, and J. Virieux, 2009a, Robust elastic frequency-domain full-waveform inversion using the L1 norm: *Geophysical Research Letters*, **36**, no. 20, L20310, [doi:10.1029/2009GL039458](https://doi.org/10.1029/2009GL039458).
- , 2009b, Which data residual norm for robust elastic frequency-domain full waveform inversion?: *Geophysics*, in press.
- Kommedal, J. H., O. I. Barkved, and D. J. Howe, 2004, Initial experience operating a permanent 4C seabed array for reservoir monitoring at Valhall: *SEG Technical Program Expanded Abstracts*, **23**, no. 1, 2239–2242, [doi:10.1190/1.1839696](https://doi.org/10.1190/1.1839696).
- Nocedal, J., 1980, Updating Quasi-Newton Matrices With Limited Storage: *Mathematics of Computation*, **35**, 773–782.
- Pratt, R. G., 1999, Seismic waveform inversion in the frequency domain, part I: theory and verification in a physic scale model: *Geophysical s*, **64**, 888–901, [doi:10.1190/1.1444597](https://doi.org/10.1190/1.1444597).
- Pratt, R. G., R. E. Plessix, and W. A. Mulder, 2001, Seismic waveform tomography: the effect of layering and anisotropy: 63rd Annual International Meeting, EAGE, Expanded Abstracts, P092.
- Pratt, R. G., and M. H. Worthington, 1990, Inverse theory applied to multi-source cross-hole tomography. Part I: acoustic waveequation method: *Geophysical Prospecting*, **38**, no. 3, 287–310, [doi:10.1111/j.1365-2478.1990.tb01846.x](https://doi.org/10.1111/j.1365-2478.1990.tb01846.x).
- Sen, M. K., and P. L. Stoffa, 1995, *Global optimization methods in geophysical inversion*: Elsevier Science Publishing Co.
- Sirgue, L., O. I. Barkved, J. Dellinger, J. Etgen, U. Albertin, and J. H. Kommedal, 2010, Full waveform inversion: the next leap forward in imaging at Valhall: *First Break*, **28**, 65–70.
- Sirgue, L., O. I. Barkved, J. P. V. Gestel, O. J. Askim, and J. H. Kommedal, 2009, 3D waveform inversion on Valhall wide-azimuth OBC: 71st Annual International Meeting, EAGE, Expanded Abstracts, U038.